

WAVE-EQUATION MIGRATION VELOCITY ANALYSIS USING
IMAGE-SPACE GENERALIZED SOURCES

A DISSERTATION
SUBMITTED TO THE DEPARTMENT OF GEOPHYSICS
AND THE COMMITTEE ON GRADUATE STUDIES
OF STANFORD UNIVERSITY
IN PARTIAL FULFILLMENT OF THE REQUIREMENTS
FOR THE DEGREE OF
DOCTOR OF PHILOSOPHY

Claudio Guerra

April 2010

© Copyright by Claudio Guerra 2009
All Rights Reserved

I certify that I have read this dissertation and that, in my opinion, it is fully adequate in scope and quality as a dissertation for the degree of Doctor of Philosophy.

(Biondo Biondi) Principal Adviser

I certify that I have read this dissertation and that, in my opinion, it is fully adequate in scope and quality as a dissertation for the degree of Doctor of Philosophy.

(Jon F. Claerbout)

I certify that I have read this dissertation and that, in my opinion, it is fully adequate in scope and quality as a dissertation for the degree of Doctor of Philosophy.

(Jerry Harris)

Approved for the University Committee on Graduate Studies.

Abstract

Preface

The electronic version of this report¹ makes the included programs and applications available to the reader. The markings **ER**, **CR**, and **NR** are promises by the author about the reproducibility of each figure result. Reproducibility is a way of organizing computational research that allows both the author and the reader of a publication to verify the reported results. Reproducibility facilitates the transfer of knowledge within SEP and between SEP and its sponsors.

ER denotes Easily Reproducible and are the results of processing described in the paper. The author claims that you can reproduce such a figure from the programs, parameters, and makefiles included in the electronic document. The data must either be included in the electronic distribution, be easily available to all researchers (e.g., SEG-EAGE data sets), or be available in the SEP data library². We assume you have a UNIX workstation with Fortran, Fortran90, C, X-Windows system and the software downloadable from our website (SEP makerules, SEPScons, SEPlib, and the SEP latex package), or other free software such as SU. Before the publication of the electronic document, someone other than the author tests the author's claim by destroying and rebuilding all ER figures. Some ER figures may not be reproducible by outsiders because they depend on data sets that are too large to distribute, or data that we do not have permission to redistribute but are in the SEP data library, or that the rules depend on commercial packages such as Matlab or Mathematica.

¹<http://sepwww.stanford.edu/private/docs/sep137>

²<http://sepwww.stanford.edu/public/docs/sepdata/lib/toc.html>

CR denotes Conditional Reproducibility. The author certifies that the commands are in place to reproduce the figure if certain resources are available. The primary reasons for the CR designation is that the processing requires 20 minutes or more.

NR denotes Non-Reproducible figures. SEP discourages authors from flagging their figures as NR except for figures that are used solely for motivation, comparison, or illustration of the theory, such as: artist drawings, scannings, or figures taken from SEP reports not by the authors or from non-SEP publications. Some 3D synthetic data examples associated with this report are classified as NR because they were generated externally to SEP and only the results were released by agreement.

Our testing is currently limited to LINUX 2.6 (using the Intel Fortran90 compiler) and the SEPlib-6.4.6 distribution, but the code should be portable to other architectures. Reader's suggestions are welcome. For more information on reproducing SEP's electronic documents, please visit <http://sepwww.stanford.edu/research/redoc/>.

Acknowledgments

Contents

Abstract	v
Preface	vi
Acknowledgments	viii
1 Introduction	1
2 Pre-Stack Exploding-Reflector Model	2

List of Tables

List of Figures

2.1	a) Shot-profile migration of 380 off-end shots 24 m apart. b) Shot-profile migration of 23 off-end shots 384 m apart. Both images were computed with the correct velocity model. Notice slanted lines present in Figure 2.1b.	5
2.2	a) Shot-profile migration of 95 areal shots resulting from the combination of 4 shot profiles 2256 m apart. b) Shot-profile migration of 23 areal shots resulting from the combination of 16 shot profiles 564 m apart. Both images were computed with the correct velocity model. Notice crosstalk occurring periodically in the SODCIG of Figure 2.2b.	6
2.3	Shot-profile migration of 401 split-spread shots 10 m apart with a 10% slower velocity. The model consists of a horizontal reflector embedded in constant velocity of 1000 m/s.	13
2.4	Data synthesized by PERM having as the initial condition the SODCIG at $x_m = 0$ m. a) The receiver wavefield. b) The source wavefield.	13
2.5	Areal-shot migration of PERM data shown in Figure 2.4 with a 10% slower velocity. By comparing with Figure 2.3 we see that far subsurface-offsets are not properly imaged.	14

2.6	Areal-shot migration of PERM data having a set of isolated SODCIGs around $x_m = 0$ m as the initial condition with a 10% slower velocity. By comparing with Figure 2.3 we see that the kinematics of far subsurface-offsets is properly recovered.	15
2.7	ADCIGs selected at $x_m = 0$ m. a) Computed from the shot-profile migration; b) computed from the areal-shot migration of one pair of PERM data modeled from the SODCIG at $x_m = 0$ m; and c) computed from the areal-shot migration of pairs of PERM data modeled from a set of SODCIGs around $x_m = 0$ m. Notice that although the kinematics are similar, the amplitudes in c) better match those of a).	16
2.8	Areal-shot migration of PERM data having a set of isolated SODCIGs around $x_m = 0$ m as the initial condition with the correct velocity. Energy nicely focuses at zero-subsurface offset.	16
2.9	Geometry for the computation of SODCIGs. Source, receiver and image points are labeled with S, R and I, respectively. The subscript hx corresponds to subsurface offsets computed with horizontal shift. The subscript hg corresponds to subsurface offsets computed by shifting along the apparent geological dip α . a) Underestimated velocity, and b) overestimated velocity. Modified from Biondi and Symes (2004).	20
2.10	Shot-profile migration of 801 split-spread shots 10 m apart with velocity 10% slower than the true velocity. The model is represented by a 20° dipping reflector and a horizontal reflector at a depth of 2500 m embedded in a medium with a constant velocity of 1000 m/s.	23
2.11	Data synthesized by PERM having as the initial condition the dipping reflector in the SODCIG at $x_m = 0$ m. a) The receiver wavefield. b) The source wavefield.	24
2.12	Areal-shot migration of PERM data shown in Figure 2.11 using the correct velocity. The horizontal reflector is focused at zero-subsurface offset, but the dipping reflector shows residual curvature.	24

2.13	Areal-shot migration with correct velocity of PERM data having a set of isolated SODCIGs around $x_m = 0$ m as the initial conditions. As in Figure 2.12, the horizontal reflector is focused at zero-subsurface offset, but the dipping reflector shows residual curvature.	25
2.14	Initial conditions for modeling a) source and b) receiver wavefields. The dipping reflector is oriented in opposite directions in the SODCIG. Rotation affects neither the horizontal reflector nor the-zero subsurface offset, as can be seen in the right panels.	26
2.15	Dip-independent PERM data for the dipping reflector from the rotated SODCIG at $x_m = 0$ m. a) The receiver wavefield. b) The source wavefield.	27
2.16	Areal-shot migration with the correct velocity of dip-independent PERM data having the rotated the SODCIGs at $x_m = 0$ m as the initial condition. Compare with Figure 2.12. The dipping reflector is now focused, in contrast to the image in Figure 2.12, where it shows residual curvature. 27	27
2.17	Areal-shot migration with correct velocity of dip-independent PERM data having a set of rotated SODCIGs around $x_m = 0$ m as the initial conditions. Compare with Figure 2.13. The focusing of the dipping reflector is greatly improved when using the rotated initial conditions. 28	28
2.18	ADCIGs of images computed with the correct migration velocity using PERM data having: a) non-rotated initial conditions, and b) rotated initial conditions. Note the residual move-out in a) and the flatter response in b).	29
2.19	Areal-shot migration of PERM data synthesized from sets of SODCIGs selected with sampling period of 163 SODCIGs. Notice that no crosstalk is generated when the sampling period is larger than twice the maximum absolute subsurface-offset.	31

2.20	The initial conditions for synthesizing PERM data from CAM images can be specified as in b) because no pre-stack information exists in the cross-line direction, in contrast with the full azimuth situation in a).	34
2.21	Common-azimuth migration of 3D-Born data modeled from a 30° dipping reflector with 45° azimuth with respect to the acquisition direction. The panel in the middle is the in-line at the zero-subsurface offset, and $y = 600$ m (Figure 2.21a) and $y = 1000$ m (Figure 2.21b). The panel on the right is the cross-line at the zero-subsurface offset, and $x = 750$ m.	35
2.22	3D-PERM receiver wavefield. The left panel is the in-line at $y = 1200$ m, the right panel is the cross-line at $x = 1400$ m, and the top panel is the time-slice at $t = 0.5$ s.	36
2.23	3D-areal-shot migration of PERM data. The panel in the middle is the in-line at the zero-subsurface offset, and $y = 600$ m (Figure 2.21a) and $y = 1000$ m (Figure 2.21b). The panel on the right is the cross-line at the zero-subsurface offset, and $x = 750$ m. Compare with Figure 2.21.	37

Chapter 1

Introduction

Chapter 2

Pre-Stack Exploding-Reflector Model

This chapter introduces the pre-stack exploding-reflector model (PERM). PERM uses *exploding* reflectors as the initial conditions to synthesize data, in a manner similar to the well-known exploding-reflector model (ERM). However, PERM also considers reflectivity as a function of subsurface-offsets, as opposed to the zero-subsurface offset initial condition used by ERM. In this sense, PERM is a generalization of ERM since wave-equation migration of PERM data can generate a pre-stack image, which is not achievable with ERM. The modeling of PERM data can be performed using any wave propagation scheme; here I use the one-way wave-equation. As in the exploding-reflector model, the modeling experiments can be combined, potentially decreasing data size by orders of magnitude when compared to the original shot records. Data size reduction is very appealing for migration velocity analysis, especially using wavefield-extrapolation methods in 3D projects. After describing the exploding-reflector concept, I generalize it by describing the theory of PERM. The usefulness of PERM to migration velocity analysis, is demonstrated through migration examples.

INTRODUCTION

Migration is applied to seismic data to generate an image of the subsurface. For many years, migration was applied only in the post-stack domain, using the idea of exploding reflectors (Loewenthal et al., 1976; Claerbout, 1985). The simple but powerful concept of the exploding-reflector model (ERM) states that a zero-offset time section can be considered as the recording at the surface of wavefields generated by simultaneous explosions of all points in the subsurface. The strength of the explosions is proportional to the reflection coefficient and, because the wavefield propagates from the subsurface to the surface, to obtain correct kinematics the medium velocity must be halved.

Migration in the post-stack domain assumes that data is transformed to some approximation of the zero-offset acquisition geometry. Because of the required transformation to zero-offset, many algorithms have been developed, including dip moveout (DMO — Hale (1984); Black and Egan (1988); Liner (1991)), migration to zero-offset (MZO — Tygel et al. (1998); Bleistein et al. (1999), and common-reflection surface (Gelchinsky, 1988; Cruz et al., 2000). DMO and MZO can be considered very particular cases of the more general azimuth moveout (AMO — (Biondi et al., 1998)), which must be applied to 3D data prior to common-azimuth migration (Biondi and Palacharla, 1996).

In fairly simple geology, ERM perfectly matches the kinematics of the zero-offset data that would have been recorded with coincident source and receivers at the surface. This means that for ERM to hold, it is necessary that the downgoing path from the source to a point in the subsurface be the same as the upgoing path from the point in the subsurface back to the receiver. However, this assumption is often invalid in areas of geological complexity. Post-stack imaging below salt bodies, for instance, can give rise to numerous migration artifacts, in the presence of prismatic and strongly refracted waves (Peles et al., 2004). Therefore, post-stack migration does not produce reliable images in the presence of strong lateral velocity variation.

In areas of complex geology, pre-stack depth migration becomes mandatory not

only for imaging purposes but also for velocity estimation. In such areas, migration by wavefield extrapolation has been widely used to produce the final image because it properly handles complex distortions of the wavefields. However, due to the high computational cost, wavefield extrapolation methods are rarely used to estimate the migration velocity model in 3D projects (Fei et al., 2009), where ray-based methods are the industry standards. In addition to the lower cost, ray-based methods are very flexible with respect to strategies for defining the velocity model (Stork, 1992; Kosloff et al., 1996, 1997; Billette et al., 1997). But despite their advantages, ray methods do not satisfactorily describe complex wave propagation in the presence of large lateral velocity contrasts. In this case, a more complete description of the wavefield complexities is needed, and therefore we face the challenge of decreasing the cost of migration velocity analysis by wavefield extrapolation while maintaining its robustness.

A typical way of decreasing the cost of wavefield extrapolation is to reduce the amount of input data. Data size can be reduced by selecting a smaller number of shots. Figure 2.1 shows pre-stack images computed with the multi-offset imaging condition (Rickett and Sava, 2002) using 380 shots 24 m apart (Figure 2.1a) and 23 shots 384 m apart (Figure 2.1b). The shot records are modeled with the one-way wave equation, using a smoothed version of the Marmousi velocity model. The same velocity model is used to migrate the data. The right panel is the zero-subsurface-offset section and the left panel is the subsurface-offset-domain common-image gather (SODCIG) selected at $x = 2760$ m on the right panel. Notice the slanted lines in the SODCIG of Figure 2.1b representing the angles according to which reflectors are illuminated. When using all the shots, the slanted lines constructively interfere and the energy is focused at zero-subsurface-offset (Figure 2.1a).

By selecting only a few shots, the migration output shows poor angular coverage. An alternate way of reducing data size is by combining shot-profiles into areal shots based on the linearity of wavefield propagation. Data is multiplied by a comb function and stacked to originate one areal shot. The comb function is shifted until all shots are selected. The original angular coverage is maintained if the period of

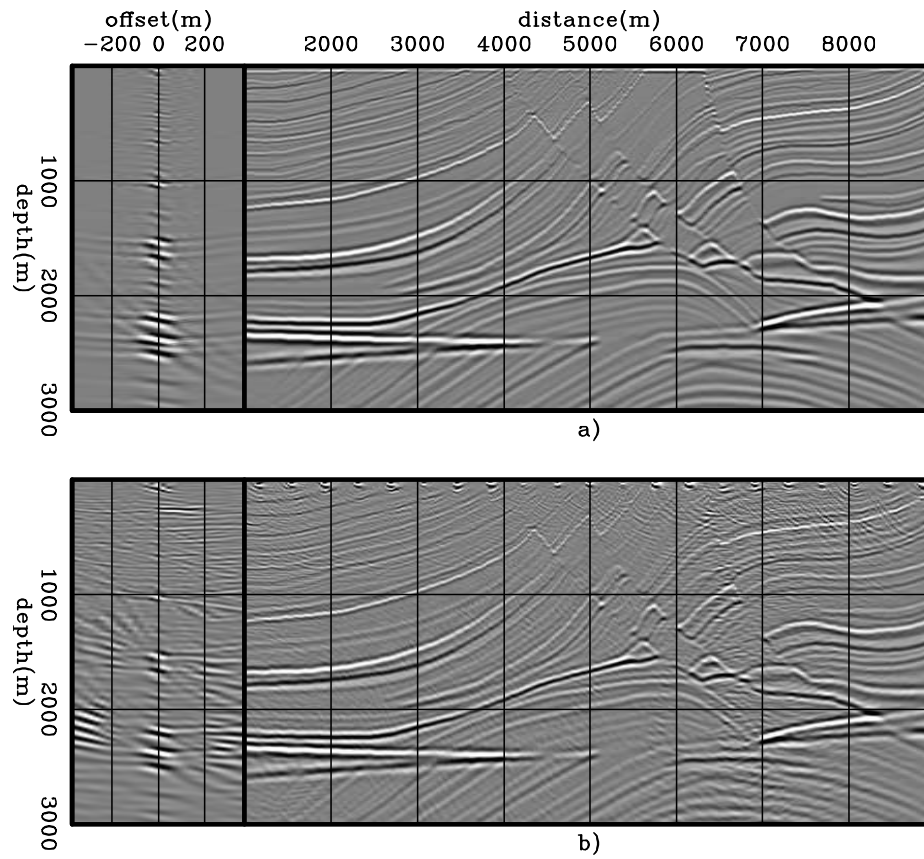


Figure 2.1: a) Shot-profile migration of 380 off-end shots 24 m apart. b) Shot-profile migration of 23 off-end shots 384 m apart. Both images were computed with the correct velocity model. Notice slanted lines present in Figure 2.1b. perm/. perm01

the sampling function is sufficiently big (Figure 2.2a). However, if many shots are combined, crosstalk is generated, since unrelated shots and receiver wavefields are cross-correlated during imaging (Figure 2.2b). Compare Figures 2.2a and 2.2b with Figure 2.1a. Crosstalk can completely overwhelm the reflectors, and the kinematic information for migration velocity analysis can be lost.

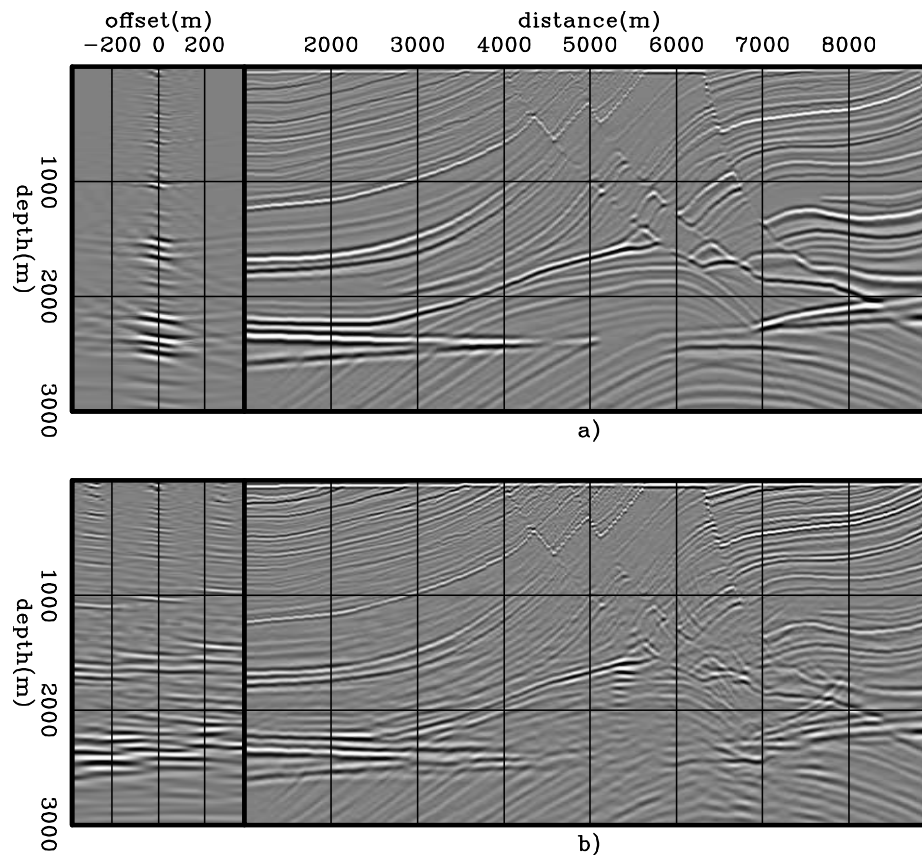


Figure 2.2: a) Shot-profile migration of 95 areal shots resulting from the combination of 4 shot profiles 2256 m apart. b) Shot-profile migration of 23 areal shots resulting from the combination of 16 shot profiles 564 m apart. Both images were computed with the correct velocity model. Notice crosstalk occurring periodically in the SOD-CIG of Figure 2.2b. `perm/. perm02`

The combination of wavefields is implicit in ERM. When reflectors are allowed to simultaneously explode, linearity of wavefield propagation is evoked to combine

wavefields initiated at every point in the subsurface. However, crosstalk is not generated in post-stack migration based on ERM since no cross-correlation of wavefields is performed; rather the imaging condition is a simple summation over frequency, which extracts the image at zero time of wavefield propagation (Claerbout, 1971). Therefore, it is natural to consider the combination of wavefields in any generalization of ERM.

Combination of wavefields is exploited by the prestack-exploding reflector model (PERM) (Biondi, 2006) to significantly reduce the data size used in migration velocity updates. Like ERM, PERM uses the concept of exploding-reflectors to propagate wavefields. However, instead of considering reflectivity only as a function of the spatial coordinates, reflectivity is also parameterized as a function of subsurface-offsets. Its elementary idea is to synthesize data necessary to correctly image a single reflector of an isolated SODCIG, so that migration of PERM data shows the correct kinematics needed for performing velocity updates.

An interesting feature of PERM is that it can be used in a target-oriented way, since the modeled data contains all the information necessary to image a predefined region of the subsurface. This concept is used in different methods, such as controlled illumination (Rietveld et al., 1992; Rietveld and Berkhout, 1992) and common-focus point (CFP) (Berkhout, 1997a,b; Thorbecke and Berkhout, 2006).

In this chapter, I introduce and further develop PERM. I will show that data synthesized with PERM has the kinematic information necessary to perform migration velocity analysis. Although, in this thesis, migration velocity analysis is performed using wave-equation tomography, ray-based tomography can also be used in conjunction with PERM data. Before introducing the theory of PERM, I will first describe the exploding-reflector concept of which PERM is a generalization. The usefulness of PERM for migration velocity analysis will be illustrated by comparing areal-shot migration of PERM wavefields with that of shot-profile migration for simple bidimensional models. The extension to a tridimensional (3D) medium is straightforward. In 3D, it will be shown that under the common-azimuth approximation (Biondi and Palacharla, 1996), PERM drastically decreases data size.

EXPLODING-REFLECTOR MODEL

To describe the exploding-reflector model (ERM) let us analyze the modeling of seismic data under the acoustic approximation. Here, we consider the Born or single-scattering approximation. This consideration leads us to a linear operator whose adjoint is the migration operator.

Let us start with the constant-density acoustic wave equation for a single temporal frequency ω

$$(\nabla^2 + \omega^2 s^2(\mathbf{x})) P(\mathbf{x}, \omega) = 0, \quad (2.1)$$

where ∇^2 is the Laplacian operator, $s(\mathbf{x})$ is the slowness field, and $P(\mathbf{x}, \omega)$ is the wavefield. Note that $\mathbf{x} = (x, y, z)$ is the vector of spatial coordinates. By introducing reflectivity as $r(\mathbf{x}) = 1 - \frac{s^2(\mathbf{x})}{s_0^2(\mathbf{x})}$, where $s_0(\mathbf{x})$ is a smooth background slowness, equation 2.1 can be written as

$$(\nabla^2 + \omega^2 s_0^2(\mathbf{x}, \omega)) P(\mathbf{x}, \omega) \approx \omega^2 s_0^2(\mathbf{x}) r(\mathbf{x}) P(\mathbf{x}, \omega). \quad (2.2)$$

The total wavefield $P(\mathbf{x}, \omega)$ can be considered as the sum of an incident background wavefield $P_0(\mathbf{x}, \omega)$ with a perturbed or scattered wavefield $\Delta P(\mathbf{x}, \omega)$. Therefore, we can write

$$(\nabla^2 + \omega^2 s_0^2(\mathbf{x})) \Delta P(\mathbf{x}, \omega) \approx \omega^2 s_0^2(\mathbf{x}) r(\mathbf{x}) P(\mathbf{x}, \omega), \quad (2.3)$$

given that the background wavefield $P_0(\mathbf{x}, \omega)$ is the solution of equation 2.2 using the background slowness $s_0(\mathbf{x})$. Notice that equation 2.3 is a non-linear relationship between $r(\mathbf{x})$ and $\Delta P(\mathbf{x}, \omega)$. A linear operator can be derived by using Green's function and the Born (weak scattering) approximation. The background Green's function $G_0(\mathbf{x}', \mathbf{x}, \omega)$ is the solution of equation 2.1 using the background slowness in

the presence of a point source $\delta(\mathbf{x} - \mathbf{x}')$ at $\mathbf{x}' = (x', y', z')$:

$$\begin{cases} (\nabla^2 + \omega^2 s_0^2(\mathbf{x})) G_0(\mathbf{x}', \mathbf{x}, \omega) = 0 \\ G_0(\mathbf{x}', \mathbf{x} = \mathbf{x}', \omega) = \delta(\mathbf{x} - \mathbf{x}') \end{cases}. \quad (2.4)$$

Multiplying equation 2.4 by $[\omega^2 s_0^2(\mathbf{x}) r(\mathbf{x}) P(\mathbf{x}, \omega)]$, integrating with respect to \mathbf{x}' over the volume V in the subsurface, and comparing the result with equation 2.3, we see that

$$\Delta P(\mathbf{x}, \omega) \approx \int_V \omega^2 s_0^2(\mathbf{x}') r(\mathbf{x}') G_0(\mathbf{x}', \mathbf{x}, \omega) P(\mathbf{x}', \omega) d\mathbf{x}'. \quad (2.5)$$

Under the weak scattering assumption, the total wavefield $P(\mathbf{x}', \omega)$ can be approximated by the background wavefield $P_0(\mathbf{x}', \omega)$, and the linear relationship between the scattered wavefield $\Delta P(\mathbf{x}, \omega)$ and reflectivity $r(\mathbf{x})$ reads

$$\Delta P(\mathbf{x}, \omega) \approx \int_V \omega^2 s_0^2(\mathbf{x}') r(\mathbf{x}') G_0(\mathbf{x}', \mathbf{x}, \omega) P_0(\mathbf{x}', \omega) d\mathbf{x}'. \quad (2.6)$$

Using equation 2.6 and assuming that the background slowness field and the reflectivity distribution are known, the scattered wavefields $\Delta P(\mathbf{x}_s, \mathbf{x}_r, \omega)$ measured by receivers at $\mathbf{x}_r = (x_r, y_r, z_r)$ due to sources located at $\mathbf{x}_s = (x_s, y_s, z_s)$ are

$$\Delta P(\mathbf{x}_s, \mathbf{x}_r, \omega) \approx \int_V \omega^2 s_0^2(\mathbf{x}) G_0(\mathbf{x}_s, \mathbf{x}, \omega) r(\mathbf{x}) G_0(\mathbf{x}, \mathbf{x}_r, \omega) d\mathbf{x}, \quad (2.7)$$

which amounts to convolving the source Green's function with the reflectivity, then with the receiver Green's function, and summing the contributions of all points within V . By using one-way propagators, we downward propagate the source wavefield, convolve it with the reflectivity, and upward propagate this result up to the surface.

Zero-offset data is obtained by selecting from $\Delta P(\mathbf{x}_s, \mathbf{x}_r, \omega)$ traces with $\mathbf{x}_s = \mathbf{x}_r$,

$$\Delta P(\mathbf{x}_s, \omega)|_{x_s=x_r} \approx \int \omega^2 s_0^2(\mathbf{x}) r(\mathbf{x}) G_0(\mathbf{x}_s, \mathbf{x}, \omega)|_{x_s=x_r} G_0(\mathbf{x}, \mathbf{x}_s, \omega) d\mathbf{x}. \quad (2.8)$$

ERM synthesizes zero-offset data by initiating virtual sources located on the reflectors. The fundamental consideration is that the downgoing and upgoing rays of a zero-offset source and receiver pair follow the same path. The exploding-reflector wavefield is propagated with half of the actual background velocity, and the virtual sources explode with strengths proportional to their reflection coefficients. Assuming that the background slowness and the reflectivity distribution are known, the wavefield generated by the exploding-reflector model $P_{ERM}(\mathbf{x}, \omega)$ propagates according to the following one-way wave-equation:

$$\begin{cases} \left(\frac{\partial}{\partial z} + i\sqrt{\omega^2 s^2(\mathbf{x}) - |\mathbf{k}|^2} \right) P_{ERM}(\mathbf{x}, \omega) = r(\mathbf{x}) \\ P_{ERM}(x, y, z = z_{\max}, \omega) = 0 \end{cases} . \quad (2.9)$$

ERM is kinematically correct only if the source and receiver Green's functions are equal for $\mathbf{x}_s = \mathbf{x}_r$ at a point \mathbf{x} in the subsurface. Notice that this condition is unlikely to be fulfilled in the presence of strong lateral velocity variations (Peles et al., 2004). Moreover, ERM does not model multiples and prismatic reflections (Claerbout, 1985).

In equation 2.9, the reflectivity $r(\mathbf{x})$ acts as the initial condition for the wavefield propagation. Notice that a migrated image can replace the reflectivity in the initial condition. Taking into consideration the imaging principle (Claerbout, 1971) and the computation of pre-stack images by wave-extrapolation methods (Claerbout, 1985; Rickett and Sava, 2002), ERM, as initially formulated, implicitly assumes that all the seismic energy is perfectly focused at zero subsurface offset and that it is sufficient to parameterize the migrated image as a function of only the position vector \mathbf{x} . This implies that the slowness field is accurate and illumination of the subsurface is sufficiently good. When this is not the case, the migrated image must be described not only as a function of \mathbf{x} , but also as a function of the subsurface offset or aperture angle.

The generalization of ERM proposed in this thesis does not aim at computing pre-stack data. Rather, it synthesizes data whose migration with wavefield-extrapolation

methods enables the computation of a pre-stack image. PERM uses the ERM concept with a poorly focused pre-stack image as the initial condition to propagate wavefields. The modeled data is, potentially, orders of magnitude smaller than the original shot records and contains all necessary kinematic information to update the velocity model using ray-based tomography or, as used in this thesis, wave-equation-based tomography. This characterizes the pre-stack-exploding-reflector model, which will be described in the next section.

PRE-STACK-EXPLODING-REFLECTOR MODEL

The fundamental idea of PERM is to model data that describes the correct kinematics of an isolated SODCIG. Many shot records contribute to form the image at a point in the subsurface. Therefore, to model data using conventional one-way modeling, we would perform several modeling experiments consisting of downward continuing the source wavefield initiated by point sources at the surface, convolving the propagated source wavefield with the SODCIG, and upward continuing the convolution result up to the surface. As we do not know beforehand which shots contribute to forming the image at a point in the subsurface, we would have to model every shot originally present in the original dataset.

Ideally, instead of performing many modeling experiments, we would like to synthesize a small amount of data with the condition that migration has the same kinematics as the initial SODCIG. This can be achieved by using a strategy similar to ERM. To compute SODCIGs using the new modeled data, we need to synthesize source and receiver wavefields.

The modeling of PERM source D_P and receiver U_P wavefields can be carried out by any wavefield-continuation scheme. Here, we use the following one-way wave equations:

$$\begin{cases} \left(\frac{\partial}{\partial z} - i\sqrt{\omega^2 s_0^2(\mathbf{x}) - |\mathbf{k}|^2} \right) D_P(\mathbf{x}, \omega; \mathbf{x}_m) = I_D(\mathbf{x}_m, \mathbf{h}) \\ D_P(x, y, z = z_{\max}, \omega; \mathbf{x}_m) = 0 \end{cases}, \quad (2.10)$$

and

$$\begin{cases} \left(\frac{\partial}{\partial z} + i\sqrt{\omega^2 s_0^2(\mathbf{x}) - |\mathbf{k}|^2} \right) U_P(\mathbf{x}, \omega; \mathbf{x}_m) = I_U(\mathbf{x}_m, \mathbf{h}) \\ U_P(x, y, z = z_{\max}, \omega; \mathbf{x}_m) = 0 \end{cases}, \quad (2.11)$$

where $I_D(\mathbf{x}_m, \mathbf{h})$ and $I_U(\mathbf{x}_m, \mathbf{h})$ is the isolated SODCIG at the horizontal location \mathbf{x}_m for a single reflector, suitable for the initial conditions for the source and receiver wavefields, respectively. The subsurface-offset \mathbf{h} can be parameterized as $\mathbf{h} = (h_x, h_y, h_z)$. In this thesis, when describing 2D problems $\mathbf{h} = (h_x)$, and for the 3D case, $\mathbf{h} = (h_x, h_y)$ without considering the computation of the vertical subsurface offset h_z as introduced by Biondi and Shan (2002). The initial conditions are obtained by rotating the original unfocused SODCIGs according to the apparent geological dip of the reflector. For dipping reflectors, this rotation maintains the velocity information needed for migration velocity analysis. The rotation of SODCIGs will be described later in this chapter. If the initial condition has energy focused at the zero-subsurface offset; if no pre-stack information is available, the pre-stack image can be parameterized only by its spatial coordinates, and PERM is equivalent to ERM.

Let us now illustrate the generation of PERM data synthesized from a single SODCIG. We start with a pre-stack image computed with shot-profile migration of 401 split-spread shots at every 10 m and maximum offset of 2250 m, using a 10% lower velocity (Figure 2.3). The model consists of one reflector at 750 m depth embedded in a medium with a constant velocity of 1000 m/s. The pre-stack image has 81 subsurface offsets ranging from -400 m to 400 m. Notice the poor focusing of energy around the zero-subsurface offset due to inaccurate velocity.

The SODCIG at $x_m = 0$ m was used as the initial condition for modeling the corresponding pair of PERM source and receiver wavefields using the same inaccurate velocity. The wavefields are upward propagated according to equations 2.10 and 2.11. The PERM data is shown in Figure 2.4. Notice that the receiver wavefield (Figure 2.4a) occurs at positive times, while the source wavefield (Figure 2.4b) occurs at negative times. According to the imaging principle (Claerbout, 1971), reflectors explode at time zero. This is the time at which the source wavefield impinges on the

reflector. Because the receiver wavefield exists after the source wavefield has reached the reflector, the areal receiver data $U_P(x, y, z = 0, \omega; \mathbf{x}_m)$ is upward propagated forward in time. For the same reason, the areal source data $D_P(x, y, z = 0, \omega; \mathbf{x}_m)$ is upward propagated backward in time.

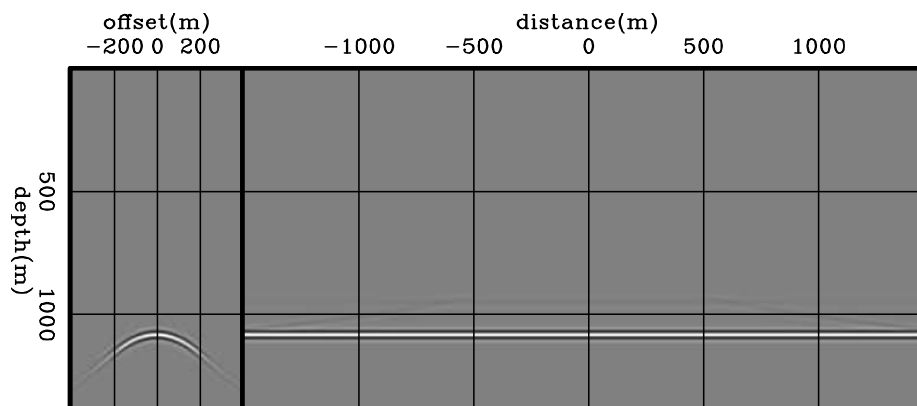


Figure 2.3: Shot-profile migration of 401 split-spread shots 10 m apart with a 10% slower velocity. The model consists of a horizontal reflector embedded in constant velocity of 1000 m/s. `perm/.refpl01`

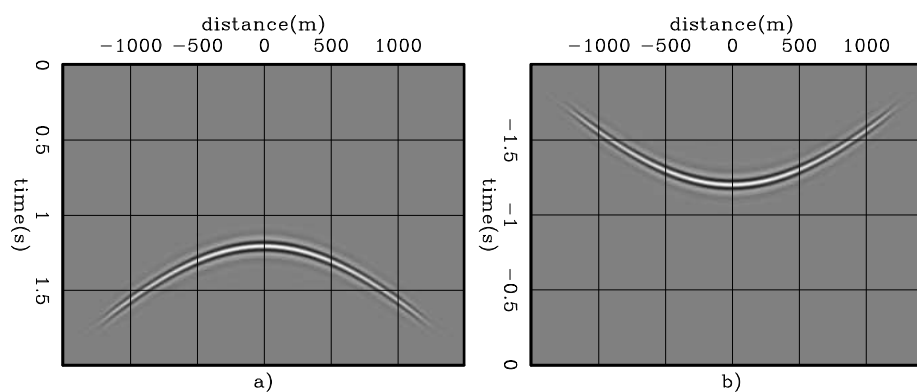


Figure 2.4: Data synthesized by PERM having as the initial condition the SODCIG at $x_m = 0$ m. a) The receiver wavefield. b) The source wavefield. `perm/.refpl02`

Areal-shot migration of data from Figure 2.4 with the same inaccurate velocity shows kinematics at near subsurface offsets similar to those of the original shot-profile migration (compare Figures 2.5 and 2.3). For farther subsurface offsets, however, energy is not adequately imaged. This can be easily explained by analyzing how an

image $I(\mathbf{x}, \mathbf{h})$ is formed when applying the multi-offset imaging condition

$$I(\mathbf{x}, \mathbf{h}) = \sum_{\omega} \sum_{\mathbf{x}_s} D^*(\mathbf{x} - \mathbf{h}, \mathbf{x}_s, \omega) U(\mathbf{x} + \mathbf{h}, \mathbf{x}_s, \omega). \quad (2.12)$$

In equation 2.12, $D(\mathbf{x} - \mathbf{h}, \mathbf{x}_s, \omega)$ and $U(\mathbf{x} + \mathbf{h}, \mathbf{x}_s, \omega)$ are the source and receiver wavefields, respectively, shifted laterally by \mathbf{h} . The image is formed by summing the contributions of all shot positions \mathbf{x}_s and all frequencies. Notice that ‘*’ stands for the complex conjugate. From equation 2.12 we can see that farther subsurface offsets get contributions from the cross-correlation of wavefields within a neighborhood around \mathbf{x} . Specifically for the PERM case, farther subsurface offsets of the areal-shot migrated image at \mathbf{x}_m (the location of the isolated SODCIG) also get contributions from the cross-correlation of wavefields generated at SODCIGs within a neighborhood around \mathbf{x}_m . Therefore, to ensure that the areal-shot migrated image has kinematics at all subsurface offsets similar to those in the original isolated SODCIG, we need to model PERM data from a set of SODCIGs around \mathbf{x}_m . From equation 2.12, it is clear that the maximum distance at which the wavefields still contribute to form the image at the maximum subsurface offset is twice the subsurface-offset range.

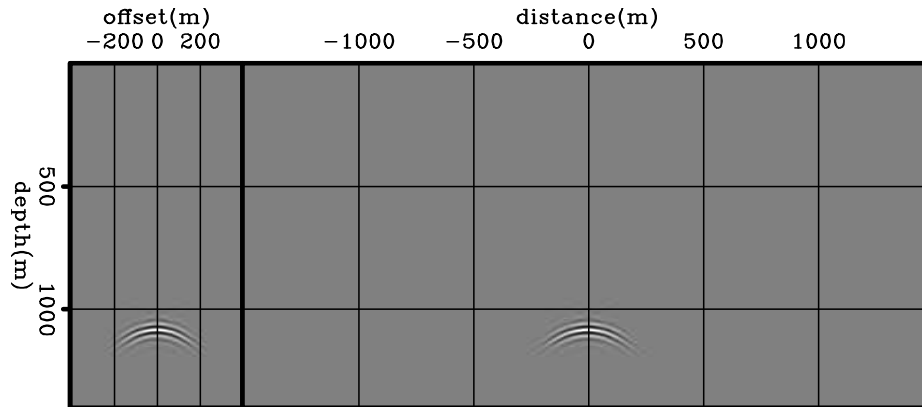


Figure 2.5: Areal-shot migration of PERM data shown in Figure 2.4 with a 10% slower velocity. By comparing with Figure 2.3 we see that far subsurface-offsets are not properly imaged. perm/. refpl03

The areal-shot migration of PERM data synthesized by isolated SODCIGs within the interval $(-2max|h_x|, 2max|h_x|)$ is shown in Figure 2.6. By using more data,

energy is adequately imaged at far subsurface offsets (compare with Figures 2.3 and 2.5). To further understand the behavior of the areal-shot migrated image, let us examine the reflection angle-domain common-image gathers (ADCIGs) (Sava and Fomel, 2003). ADCIGs computed from the SODCIGs of Figures 2.3, 2.5 and 2.6 attest to the more accurate imaging when migrating data modeled from the set of SODCIGs around \mathbf{x}_m (Figure 2.7). Although the ADCIG from the the image computed with a single pair of PERM data (Figure 2.7b) shows reasonable kinematics, the amplitude of wide-aperture angles is weaker than that of the original ADCIG (Figure 2.7a). Notice that the amplitude behavior of the ADCIG computed with several areal shots from SODCIGs within the neighborhood of \mathbf{x}_m (Figure 2.7c) better matches that of the original isolated SODCIG.

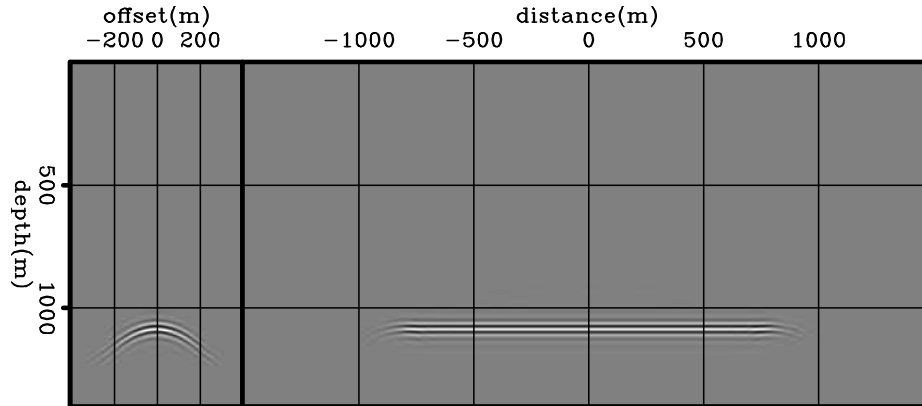


Figure 2.6: Areal-shot migration of PERM data having a set of isolated SODCIGs around $x_m = 0$ m as the initial condition with a 10% slower velocity. By comparing with Figure 2.3 we see that the kinematics of far subsurface-offsets is properly recovered. `perm/.refpl04`

If, instead of using the incorrect migration velocity, we input the correct migration velocity to the areal-shot migration, energy nicely focuses at zero subsurface offset (Figure 2.8). This property will be used to perform migration velocity updates in Chapter 3.

In the previous examples we saw that PERM data contains all the kinematic information needed to perform migration velocity analysis. However, by carefully examining the migration results of the original data and PERM data we can see that

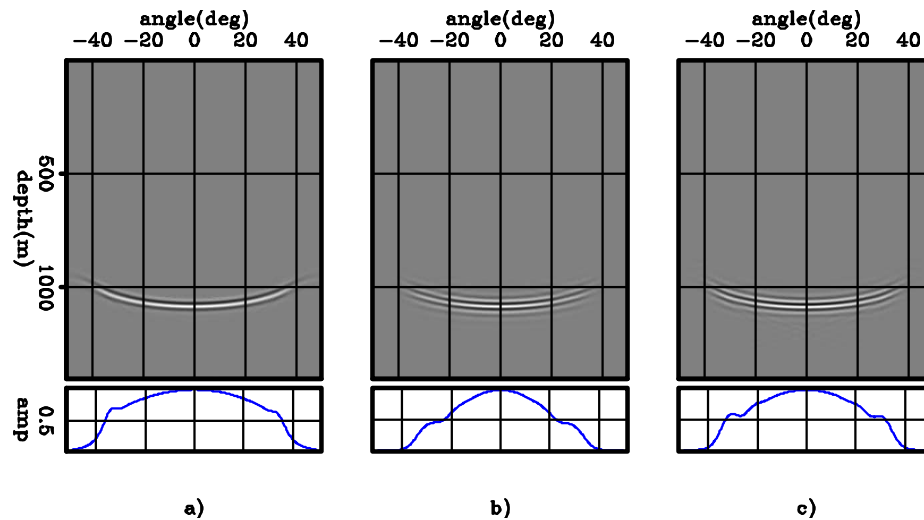


Figure 2.7: ADCIGs selected at $x_m = 0$ m. a) Computed from the shot-profile migration; b) computed from the areal-shot migration of one pair of PERM data modeled from the SODCIG at $x_m = 0$ m; and c) computed from the areal-shot migration of pairs of PERM data modeled from a set of SODCIGs around $x_m = 0$ m. Notice that although the kinematics are similar, the amplitudes in c) better match those of a). `perm/.refpl05`

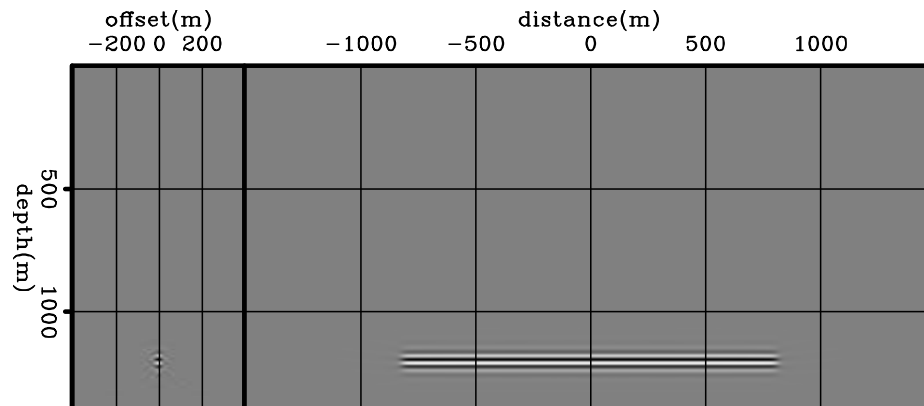


Figure 2.8: Areal-shot migration of PERM data having a set of isolated SODCIGs around $x_m = 0$ m as the initial condition with the correct velocity. Energy nicely focuses at zero-subsurface offset. `perm/.refpl06`

the latter has stronger side lobes.

The stronger side lobes are due to the squaring of the wavelet. It occurs because PERM source and receiver wavefields contain the waveform of the original image. Let us consider, for simplicity, a plane reflector so that the initial conditions are the same for modeling source D_P and receiver U_P wavefields. For only one frequency, PERM can be described by

$$D_P(\boldsymbol{\xi}) = \mathcal{L}_0(\boldsymbol{\xi}, \mathbf{x} - \mathbf{h})I(\mathbf{x}, \mathbf{h}), \quad (2.13)$$

and

$$U_P(\boldsymbol{\xi}) = \mathcal{L}_0(\boldsymbol{\xi}, \mathbf{x} + \mathbf{h})I(\mathbf{x}, \mathbf{h}). \quad (2.14)$$

The operator \mathcal{L} is the recursive upward propagation of the wavefields from the subsurface (represented by the the coordinates \mathbf{x}) up to the surface (represented by the coordinates $\boldsymbol{\xi}$). This operator is also a function of the subsurface offset, because of the way the pre-stack image is injected into the modeling. The subscript of \mathcal{L} denotes that the wavefield propagation is performed with the background slowness $s_0(\mathbf{x})$ used to migrate the original shot-profiles. The source wavefield is upward propagated backwards in time, and the receiver wavefield is upward propagated forward in time.

The pre-stack image I_P is computed with PERM data, at every depth level, using the multi-offset imaging condition

$$I_P(\mathbf{x}, \mathbf{h}) = D_P^*(\mathbf{x} - \mathbf{h})U_P(\mathbf{x} + \mathbf{h}). \quad (2.15)$$

The wavefields in depth are recursively downward propagated according to

$$D_P(\mathbf{x}) = \mathcal{L}'_1(\boldsymbol{\xi}, \mathbf{x})D_P(\boldsymbol{\xi}), \quad (2.16)$$

and

$$U_P(\mathbf{x}) = \mathcal{L}'_1(\boldsymbol{\xi}, \mathbf{x})U_P(\boldsymbol{\xi}). \quad (2.17)$$

where $'$ stands for the adjoint operator. Note that in equations 2.16 and 2.17 the subscript of the operator \mathcal{L} indicates the use of a different migration velocity. The source wavefield is downward propagated forward in time, and the receiver wavefield is downward propagated backwards in time. Inserting equation 2.13 into equation 2.16 and equation 2.14 into equation 2.17, and substituting the expressions for the wavefields in depth into equation 2.15, we get

$$\begin{aligned} I_P(\mathbf{x}, \mathbf{h}) &= \{\mathcal{L}'_0(\boldsymbol{\xi}, \mathbf{x} - \mathbf{h})\mathcal{L}_1(\boldsymbol{\xi}, \mathbf{x} - \mathbf{h})I(\mathbf{x}, \mathbf{h})\} \\ &\times \{\mathcal{L}'_1(\boldsymbol{\xi}, \mathbf{x} + \mathbf{h})\mathcal{L}_0(\boldsymbol{\xi}, \mathbf{x} + \mathbf{h})I(\mathbf{x}, \mathbf{h})\}. \end{aligned} \quad (2.18)$$

From equation 2.18, we can see that the pre-stack image I_P is approximately a squared version of the original image. This means that in addition to the stronger side lobes, reflectors in the PERM image will always have positive polarity.

For the simple case of a horizontal reflector in a constant velocity medium, we have shown that migration of PERM data produces images with the same kinematics as the shot profile migration. Now, we introduce a dipping reflector in the same constant background velocity medium. In the presence of a non-zero geological dip, a pre-processing of the initial conditions is necessary to obtain correct kinematics. This pre-processing step is represented by a rotation of the pre-stack image according to the apparent geological dip.

Dip-independent initial conditions

Shot-profile and areal-shot migrations by wavefield extrapolation compute pre-stack images by means of the multi-offset imaging condition (Rickett and Sava, 2002), in which source and receiver wavefields are laterally shifted prior to time correlation. However, the shift between wavefields might not be restricted to the horizontal direction. For instance, vertical shifts of the wavefields produce the vertical-subsurface-offset gathers, which provide reliable velocity information in the presence of steep dips (Biondi and Shan, 2002).

Ideally, wavefields should be shifted along the geological dip direction. According

to Biondi and Symes (2004), SODCIGs computed this way do not suffer from image-point dispersal in the presence of dip and inaccuracies in the migration velocity. The image-point dispersal causes events with different reflection angles from the same reflection point in the subsurface to be imaged at different locations.

The image-point dispersal in 2D is illustrated in Figure 2.9 for the case of migrating with a velocity slower (Figure 2.9a) and faster (Figure 2.9b) than the true velocity. For simplicity, let us consider constant velocity in the vicinity of the image point, so source and receiver rays are straight.

When the migration velocity is too low, the reflector is imaged at a shallower depth. The image point computed with horizontal shifts of the wavefields l_{hx} is shifted down-dip with respect to the image point computed with shifts along the apparent geological dip l_{hg} . The geological dip is called apparent because of the migration velocity error. The point l is where source and receiver rays cross at an angle that is twice the apparent reflection angle γ . Source and receiver rays cross deeper than the image points, causing events to curve downward in the SODCIG.

When the migration velocity is too high, the reflector is imaged at a greater depth. The image point l_{hx} is shifted up-dip with respect to l_{hg} . Source and receiver rays cross shallower than the image points, causing events to curve upward in the SODCIG.

Generating SODCIGs along the geological-dip direction overcomes the problem of the image-point dispersal. However, it is computationally demanding since, wavefields must be stored at various depths. Furthermore, accurate dip information is difficult to obtain, especially when events cross because of velocity inaccuracy.

Biondi and Symes (2004) point out that, at least to the first order, the reflection-angle domain is immune to image-point dispersal. This is because the SODCIG to ADCIG transformation shifts events to the line connecting l and l_{hg} in Figure 2.9 at the same image point shared by all the reflection angles.

In the presence of dip, to accurately model PERM data it is crucial that the initial conditions are free of image-point dispersal, so that all the energy of a point in the subsurface is contained by the corresponding SODCIG injected into the modeling.

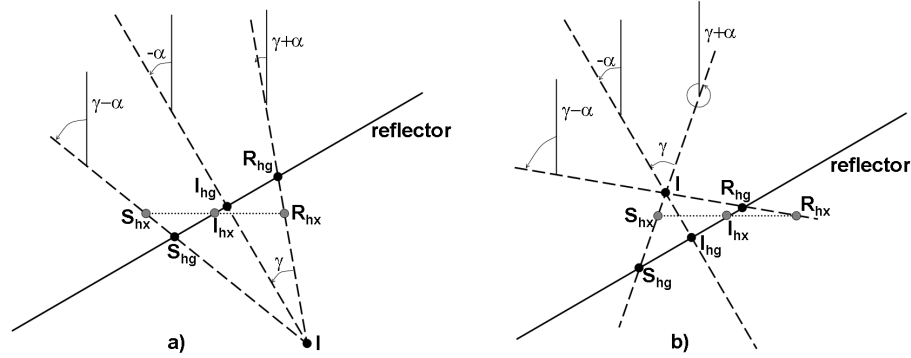


Figure 2.9: Geometry for the computation of SODCIGs. Source, receiver and image points are labeled with S, R and I, respectively. The subscript *hx* corresponds to subsurface offsets computed with horizontal shift. The subscript *hg* corresponds to subsurface offsets computed by shifting along the apparent geological dip α . a) Underestimated velocity, and b) overestimated velocity. Modified from Biondi and Symes (2004). `perm/. pdisp`

Since SODCIGs along the geological dip are not easily computed, can we pre-process the SODCIGs computed with horizontal shifts of the wavefields such that they are transformed into a good approximation of the SODCIGs along the geological dip?

To answer this question, let us first examine the angle relationships in Figure 2.9. The angles $\gamma + \alpha$ and $\gamma - \alpha$ are the source and receiver ray angles, respectively. They are the propagation directions of the wavefields locally at the image point. Notice that α and γ are related to slopes in the pre-stack image according to

$$\tan \alpha = -\frac{dz_m}{dx_m} \quad (2.19)$$

and

$$\tan \gamma = -\frac{dz}{dh_x}, \quad (2.20)$$

where the subscript *m* refers to the local nature of the relationship. The solutions of the differential equations 2.19 and 2.20 define slant-stack paths, which allow us to

transform the 2D pre-stack image $I(x, z, h_x)$ into $I(x, z, \alpha, \gamma)$ by angle decomposition according to the following integrals:

$$I(x, z, \alpha, \gamma) = \int_{x_{m_i}}^{x_{m_f}} \int_{-h_x}^{h_x} W(x_m - x) \frac{dI(x, z, h_x)}{dz} dx_m dh_x \Bigg|_{\substack{z=z_h+h_x \tan \gamma \\ z=z_m+x_m \tan \alpha}} \quad (2.21)$$

where the derivative with respect to z is performed to recover the correct phase. The local window $W(x_m - x)$ is used in the local slant-stack integral on x_m , being defined as

$$\begin{cases} 1, & x_{m_i} \leq x \leq x_{m_f}, \\ 0, & \text{elsewhere} \end{cases}$$

where $x_{m_i} = x_m - \frac{x_w}{2}$ and $x_{m_f} = x_m + \frac{x_w}{2}$, with x_w being the width of the local window.

Again, using simple trigonometry, we have

$$\tan(\gamma + \alpha) = \frac{\tan \gamma + \tan \alpha}{1 - \tan \gamma \tan \alpha}, \quad (2.22)$$

$$\tan(\gamma - \alpha) = \frac{\tan \gamma - \tan \alpha}{1 + \tan \gamma \tan \alpha}. \quad (2.23)$$

To align the initial conditions with the geological dip, we need to change the dip along the subsurface-offset axis according to the apparent geological dip, yielding the new subsurface offset $\widetilde{h_{x_s}}$ and $\widetilde{h_{x_r}}$ for the initial conditions of the modeling of source and receiver wavefield, respectively. This is accomplished by solving the following differential equations:

$$\tan(\gamma + \alpha) = -\frac{dz}{d\widetilde{h_{x_s}}}, \quad (2.24)$$

$$\tan(\gamma - \alpha) = \frac{dz}{d\widetilde{h}_{x_r}}. \quad (2.25)$$

The solutions of equations 2.24 and 2.25 define new slant-stack operations which, in combination with equations 2.22 and 2.23, reduce the dimensionality of the decomposed pre-stack image (equation 2.26) by transforming $I(x, z, \alpha, \gamma)$ into $I_D(x, z, \widetilde{h}_{x_s})$ and $I_U(x, z, \widetilde{h}_{x_r})$.

In 3D, we must also consider rotation of the cross-line offsets according to the apparent geological dip in the cross-line direction in addition to the in-line rotation. To apply the rotation in 3D, we need to assume that source and receiver rays are coplanar, such that they cross. In 3D, this assumption might not be valid when migrating with an inaccurate velocity in complex overburden. The co-planarity assumption is also present in the formulation of the common-azimuth migration (Biondi and Palacharla, 1996), which turned out to provide sufficiently accurate images in areas of complex geology.

Instead of performing a true 3D slant-stack, which can require excessive computer memory, we can take advantage of the fact that a 3D slant-stack can be split into two 2D slant-stacks on the in-line and cross-line directions. This can be easily seen by using Fourier transforms to conveniently express a generic 3D slant-stack integral

$$\begin{aligned} U(\phi_1, \phi_2, \phi_3) &= \int \int u(z, x, y) dx dy \Big|_{t=\phi_1+\phi_2x+\phi_3y} \\ &= \int \int u(\phi_1 + \phi_2x + \phi_3y, x, y) dx dy \end{aligned} \quad (2.26)$$

as

$$U(\phi_1, \phi_2, \phi_3) = \int d\phi_1 e^{-ik\phi_1} \int dx e^{-i\phi_2x} \int dy e^{-i\phi_3y} \int dz e^{ikz} u(z, x, y). \quad (2.27)$$

where ϕ_1 , ϕ_2 and ϕ_3 are, respectively, the output z , the slanting parameter corresponding to x , and the slanting parameter corresponding to y .

To illustrate the generation of dip-independent initial conditions, 801 split-spread shots 10 m apart with maximum offset of 3250 m were modeled with a velocity of 1000 m/s and migrated with velocity underestimated by 10% (Figure 2.10). The

model has a 20° dipping reflector and a horizontal reflector at a depth of 2500 m. The SODCIG located at 0 m was used as the initial condition for the modeling of PERM data without applying the pre-processing described above. Since PERM models one event of one isolated SODCIG, the dipping reflector and the horizontal reflector originate two different pairs of PERM wavefields. This means that reflectors used in the modeling need to be interpreted in the pre-stack volume. The pair of source and receiver wavefields for the dipping reflector are shown in Figure 2.11.

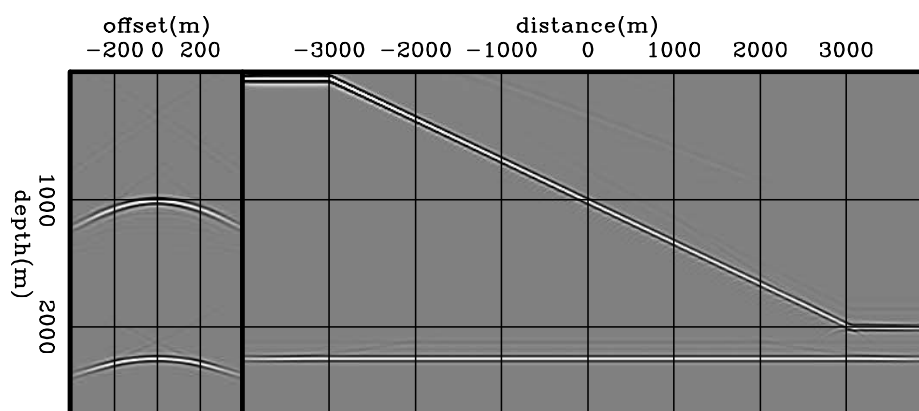


Figure 2.10: Shot-profile migration of 801 split-spread shots 10 m apart with velocity 10% slower than the true velocity. The model is represented by a 20° dipping reflector and a horizontal reflector at a depth of 2500 m embedded in a medium with a constant velocity of 1000 m/s. `perm/. dip01`

Since the modeling of a single non-rotated SODCIG carries no dip information, migration of the corresponding PERM data using the correct velocity does not shift events laterally, as can be seen in Figure 2.12. As expected, the horizontal reflector focuses at zero-subsurface offset. However, notice how the dipping reflector still presents a residual curvature. Migration of PERM data from SODCIGs within a neighborhood around $x_m = 0$ m is shown in Figure 2.13. Again, the residual curvature is present and any migration velocity analysis using this result will lead to incorrect velocity updates. This residual curvature is a result of not having corrected the image-point dispersal. Unless stated, SODCIGs in the figures are selected at $x = 0$ m.

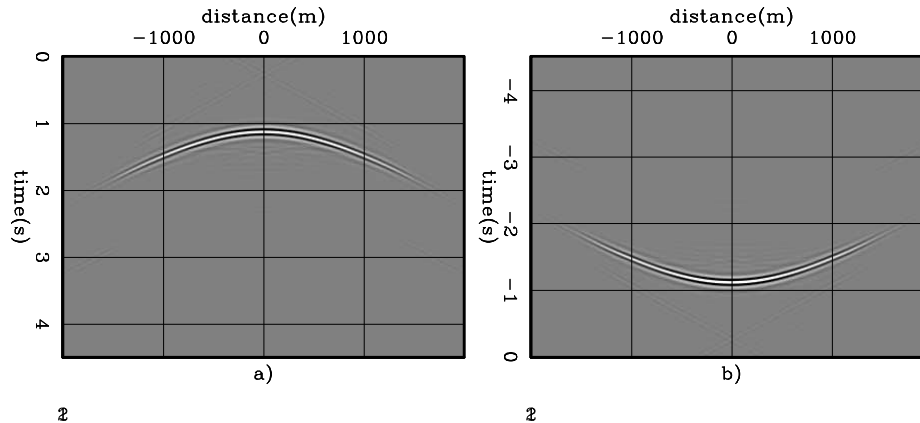


Figure 2.11: Data synthesized by PERM having as the initial condition the dipping reflector in the SODCIG at $x_m = 0$ m. a) The receiver wavefield. b) The source wavefield. `perm/. dip02`

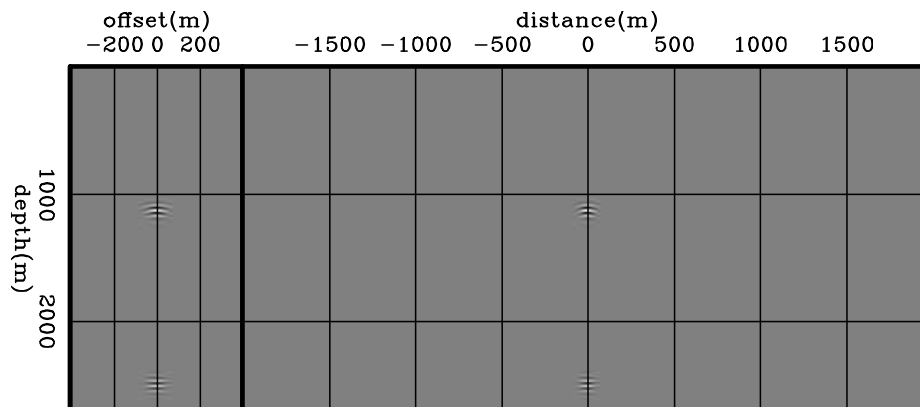


Figure 2.12: Areal-shot migration of PERM data shown in Figure 2.11 using the correct velocity. The horizontal reflector is focused at zero-subsurface offset, but the dipping reflector shows residual curvature. `perm/. dip03`

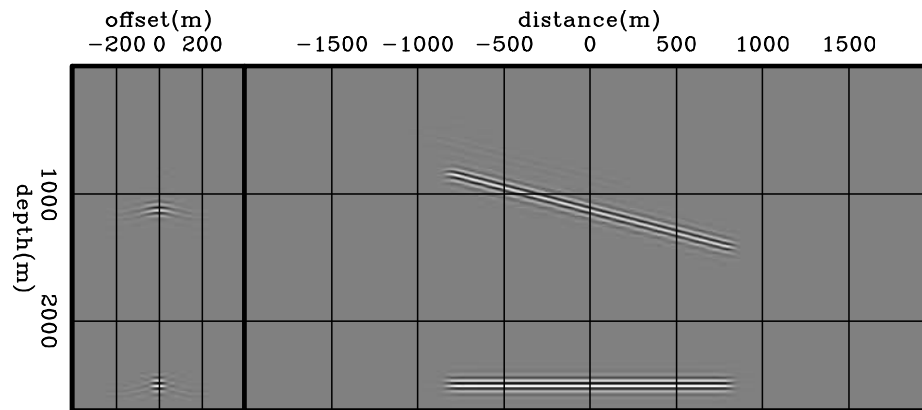


Figure 2.13: Areal-shot migration with correct velocity of PERM data having a set of isolated SODCIGs around $x_m = 0$ m as the initial conditions. As in Figure 2.12, the horizontal reflector is focused at zero-subsurface offset, but the dipping reflector shows residual curvature. `perm/. dip04`

The rotation was applied to the image in Figure 2.10, and the new PERM data was modeled using the initial conditions shown in Figure 2.14. Notice that the initial condition for modeling the source wavefield (Figure 2.14a) and the initial condition for modeling the receiver wavefield (Figure 2.14b) have the dipping event oriented in opposite directions in the SODCIG. The rotation changes neither the horizontal reflector nor the-zero subsurface offset, as can be seen in the right panels.

The source and receiver wavefields for the dipping reflector after rotation are shown in Figure 2.15. The events in Figures 2.15a and 2.15b are shown in the same areal shot for illustration only. Actually, they pertain to different areal shots.

Areal-shot migration of dip-independent PERM data is shown in Figure 2.16. Notice that the segment of the dipping reflector is shifted laterally with respect to that of the horizontal reflector. Since the dip-independent wavefields carry information about the dip of the reflector, the observed reflector movement is now consistent with migration with a higher velocity.

Migration with the correct velocity of dip-independent PERM data modeled from a set of SODCIGs in a neighborhood around $x_m = 0$ m confirms the correctness of

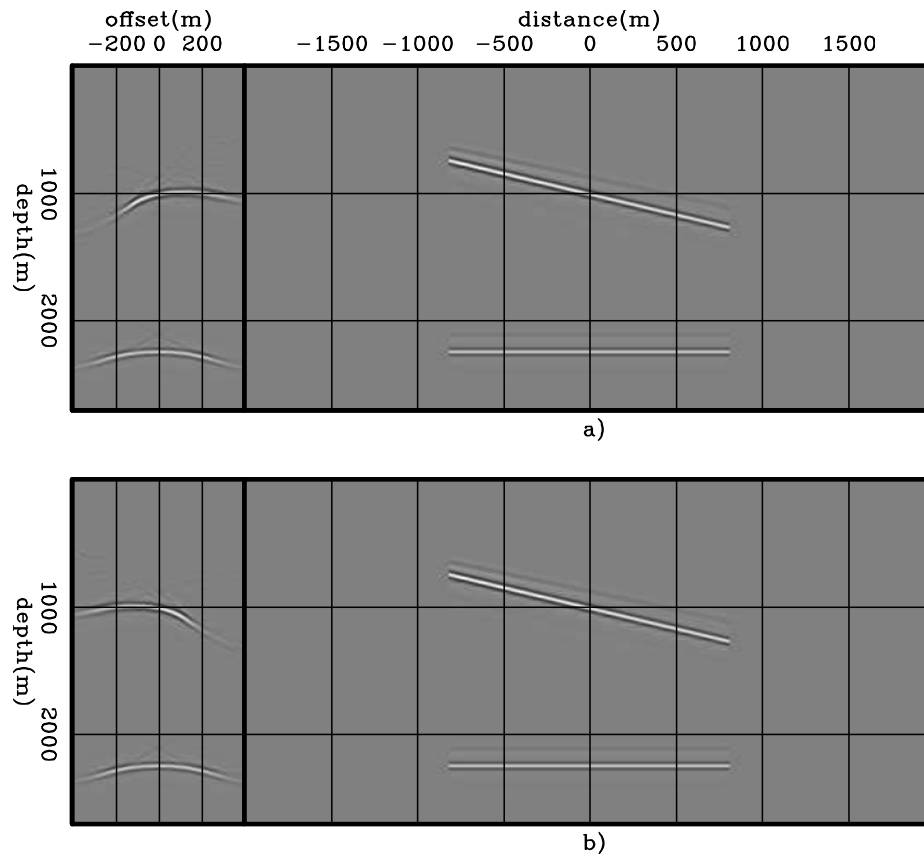


Figure 2.14: Initial conditions for modeling a) source and b) receiver wavefields. The dipping reflector is oriented in opposite directions in the SODCIG. Rotation affects neither the horizontal reflector nor the-zero subsurface offset, as can be seen in the right panels. `perm/. dip05`

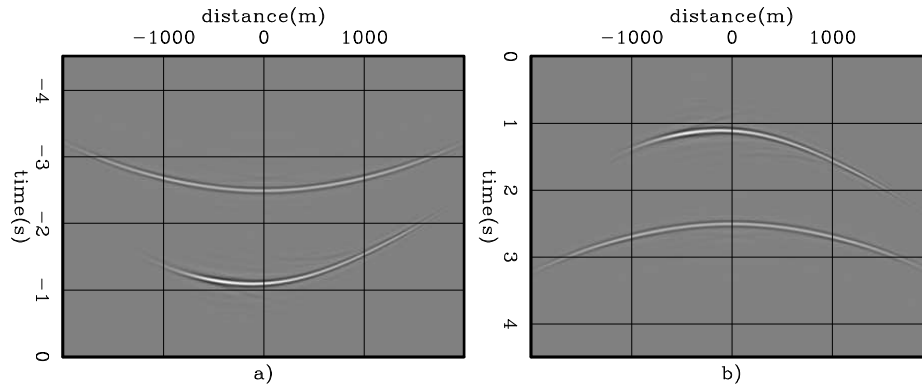


Figure 2.15: Dip-independent PERM data for the dipping reflector from the rotated SODCIG at $x_m = 0$ m. a) The receiver wavefield. b) The source wavefield.

perm/. dip06

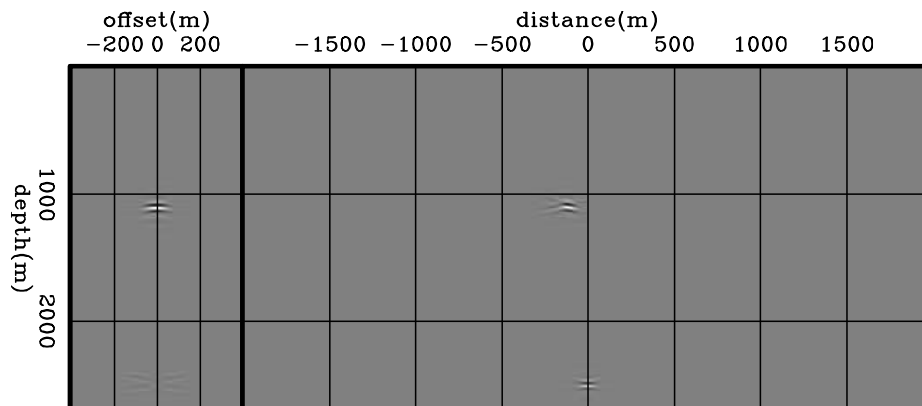


Figure 2.16: Areal-shot migration with the correct velocity of dip-independent PERM data having the rotated the SODCIGs at $x_m = 0$ m as the initial condition. Compare with Figure 2.12. The dipping reflector is now focused, in contrast to the image in Figure 2.12, where it shows residual curvature. perm/. dip07

the rotation (Figure 2.17). The focusing of the dipping reflector around zero subsurface offset is greatly improved when compared with Figure 2.13. The corresponding ADCIGs confirm the more consistent move-out after rotation (Figure 2.18). Note the residual move-out in the angle gather corresponding to the image computed with wavefields with non-rotated initial conditions (Figure 2.18a), and the image from wavefields computed with the proposed rotation is much flatter (Figure 2.18b).

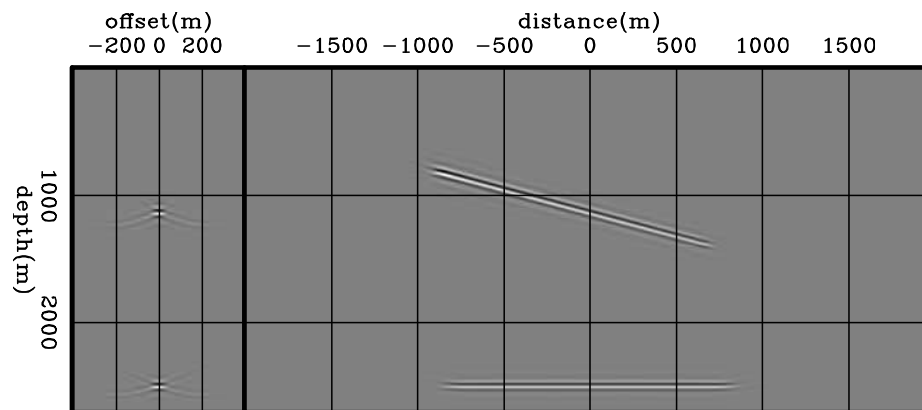


Figure 2.17: Areal-shot migration with correct velocity of dip-independent PERM data having a set of rotated SODCIGs around $x_m = 0$ m as the initial conditions. Compare with Figure 2.13. The focusing of the dipping reflector is greatly improved when using the rotated initial conditions. `perm/. dip08`

In the example with two reflectors, we initiated each modeling experiment from one isolated SODCIG of one single reflector to compute a pre-stack image restricted to a certain region in the output space. However, depending on the number of reflectors and the size of the prestack image, this procedure can generate a dataset even larger than the original shot-profiles, defeating the original purpose of PERM, which is to synthesize a smaller dataset to be used in migration velocity analysis. We see next that using a combination of modeling experiments can decrease the size of PERM data.

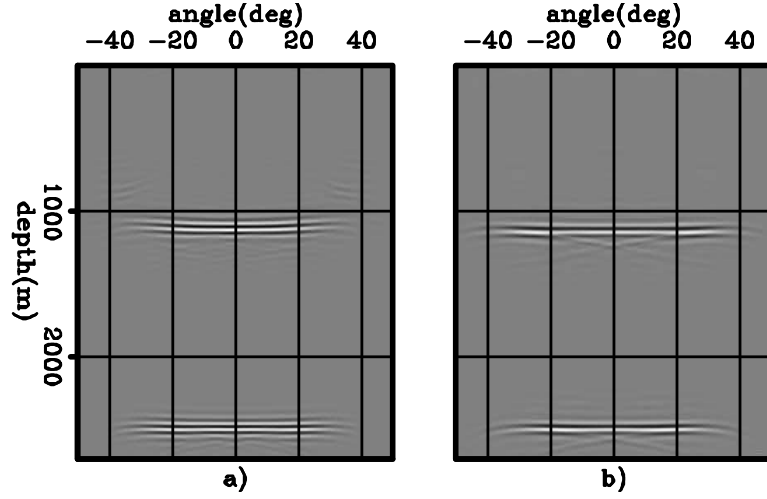


Figure 2.18: ADCIGs of images computed with the correct migration velocity using PERM data having: a) non-rotated initial conditions, and b) rotated initial conditions. Note the residual move-out in a) and the flatter response in b). perm/. dip09

Combination of modeling experiments

In the previous examples, if we were to fully image the reflectors, there might be twice as many areal shots as in the original shot-profiles. To decrease the number of modeling experiments, linearity of wave propagation can be used to combine isolated SODCIGs and inject them simultaneously into one single model experiment as

$$\left\{ \begin{array}{l} \left(\frac{\partial}{\partial z} - i\sqrt{\omega^2 s_0^2(\mathbf{x}) - |\mathbf{k}|^2} \right) \widehat{D}_P(\mathbf{x}, \omega; \widehat{\mathbf{x}}, \Delta \mathbf{x}) = \widehat{I}_D(\widehat{\mathbf{x}}; \Delta \mathbf{x}) \\ \widehat{D}_P(x, y, z = z_{\max}, \omega; \widehat{\mathbf{x}}, \Delta \mathbf{x}) = 0 \end{array} \right. , \quad (2.28)$$

and

$$\left\{ \begin{array}{l} \left(\frac{\partial}{\partial z} + i\sqrt{\omega^2 s_0^2(\mathbf{x}) - |\mathbf{k}|^2} \right) \widehat{U}_P(\mathbf{x}, \omega; \widehat{\mathbf{x}}, \Delta \mathbf{x}) = \widehat{I}_U(\widehat{\mathbf{x}}; \Delta \mathbf{x}) \\ \widehat{U}_P(x, y, z = z_{\max}, \omega; \widehat{\mathbf{x}}, \Delta \mathbf{x}) = 0 \end{array} \right. , \quad (2.29)$$

where $\widehat{I}_D(\widehat{\mathbf{x}}; \Delta \mathbf{x})$ and $\widehat{I}_U(\widehat{\mathbf{x}}; \Delta \mathbf{x})$ are the combination of SODCIGs for a single reflector to be used as the initial conditions for the modeling of combined wavefields,

$\widehat{D}_P(\mathbf{x}, \omega; \widehat{\mathbf{x}}, \Delta\mathbf{x})$ and $\widehat{U}_P(\mathbf{x}, \omega; \widehat{\mathbf{x}}, \Delta\mathbf{x})$, the source and receiver wavefields, respectively. The selection of SODCIGs can be thought of as the multiplication of the pre-stack image by 2D *Comb* functions

$$\widehat{I}_D(\widehat{\mathbf{x}}; \Delta\mathbf{x}) = Comb_D(\widehat{\mathbf{x}}; \Delta\mathbf{x}, \mathbf{x}, \mathbf{h})I_D(\mathbf{x}, \mathbf{h}), \quad (2.30)$$

and

$$\widehat{I}_U(\widehat{\mathbf{x}}; \Delta\mathbf{x}) = Comb_U(\widehat{\mathbf{x}}; \Delta\mathbf{x}, \mathbf{x}, \mathbf{h})I_U(\mathbf{x}, \mathbf{h}), \quad (2.31)$$

with period $\Delta\mathbf{x} = (\Delta x, \Delta y)$, where

$$Comb_D(\widehat{\mathbf{x}}; \Delta\mathbf{x}, \mathbf{x}, \mathbf{h}) = \sum_{m_x} \sum_{m_y} \delta(x - m_x\Delta x - h_x - \widehat{x}, y - m_y\Delta y - h_y - \widehat{y}),$$

and

$$Comb_U(\widehat{\mathbf{x}}; \Delta\mathbf{x}, \mathbf{x}, \mathbf{h}) = \sum_{m_x} \sum_{m_y} \delta(x - m_x\Delta x + h_x - \widehat{x}, y - m_y\Delta y + h_y - \widehat{y}).$$

The sampling function is shifted laterally to select new set of SODCIGs to initiate the modeling of another pair of combined wavefields. After shifting along one period of the sampling function in the x and y directions, all the points on the reflector are used in the modeling. Consequently, the number of modeling experiments equals the number of lateral shifts of the sampling function.

The choice of the sampling period determines how much crosstalk will be present in the migrated image, in a manner similar to the shot-profile migration illustrated in the introduction of this chapter. To obtain a crosstalk-free image, the sampling period must be large enough that wavefields initiated at different SODCIGs do not correlate. As previously shown when discussing how to compute PERM images with kinematics similar to those of the original shot-profile migration, PERM wavefields generated from SODCIGs within an interval equals to twice the subsurface-offset range still contribute to the image at the central SODCIG. For the same reason, no crosstalk is

generated during migration if the period of the sampling function is larger than that interval. Since the focusing of energy in the SODCIG is velocity-error dependent, so is the the period of the sampling function. Therefore, for small velocity errors a small sampling period can be used and, consequently, a smaller number of combined modeling experiments is needed.

The combination of modeling experiments is illustrated in Figure 2.19. We model PERM data starting with the rotated images from the previous section and combine SODCIGs into sets using the sampling period of 163 SODCIGs. Recalling that the number of subsurface-offsets is 81, it is expected that no crosstalk will occur when migrating the set with sampling period of 163 SODCIGs. In this case, since each reflector is used separately in the modeling, the total number of areal shots is 326, which is less than half of the original shot profiles.

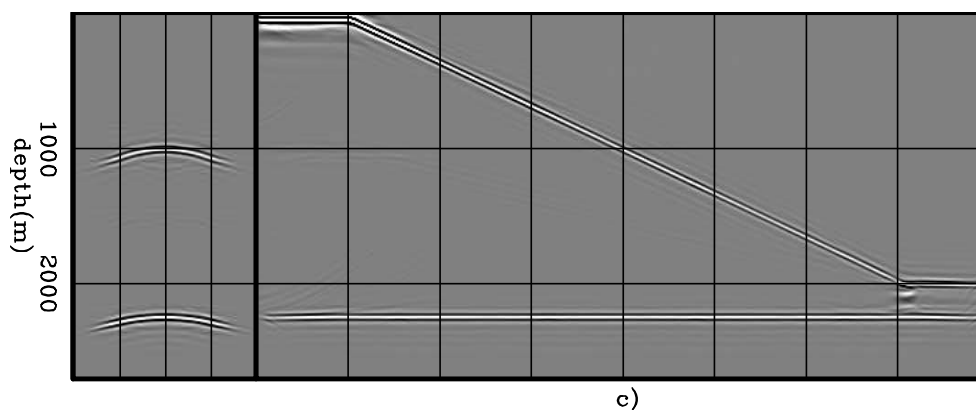


Figure 2.19: Areal-shot migration of PERM data synthesized from sets of SODCIGs selected with sampling period of 163 SODCIGs. Notice that no crosstalk is generated when the sampling period is larger than twice the maximum absolute subsurface-offset. `perm/. comb01b`

We saw that carefully combining the modeling experiments decreases the data size while maintaining the correct kinematics, which is important for migration velocity analysis. However, combining the modeling experiments using a decorrelation distance between events does not achieve a significant data reduction, at least in 2D. In

this case, data reduction depends on the number of subsurface-offsets which are necessary to capture all the relevant velocity information. In the example, the number of independent experiments is only less than one half as many as in the original dataset. Data reduction techniques like plane-wave decomposition, for instance, could lower data size by a factor of ten. As we will see in Chapter ??, further data reduction can be achieved by using the phase-encoding technique (Romero et al., 2000) to linearly combine the modeling experiments. This will enable us to use a shorter sampling period of SODCIGs, and also to inject more than one reflector in the modeling.

Although PERM theory was developed in 3D, all the examples I have shown so far have been 2D. Next, I discuss a 3D example under the common-azimuth approximation (Biondi and Palacharla, 1996) and show that in this case the SODCIGs in the y direction can be continuously sampled, and the number of modeling experiments will depend only on the sampling period in the x direction, drastically decreasing data size.

3D-PERM from common-azimuth migrated images

In the way PERM is formulated there is no restriction on the dimensionality of the pre-stack image used as the initial condition for the modeling, which means that if the original data have sufficient cross-line offsets as in the acquisition geometries with wide range of azimuths (Regone, 2007; Kapoor et al., 2007; Moldoveanu et al., 2008), the initial conditions are a five-dimensional hypercube on \mathbf{x} , h_x and h_y .

To synthesize PERM data starting with the five-dimensional initial conditions such that no crosstalk is generated during migration, the minimum number of modeling experiments is $4n_{h_x}n_{h_y}$, where n_{h_x} and n_{h_y} are the number of subsurface offsets in the x and y directions. Considering usual parameters, the number of modeling experiments may be as low as several hundreds. This data reduction is very substantial if we compare, for instance, with data reduction achieved by 3D-plane-wave migration. Using plane waves, to obtain artifact-free SODCIGs due to the lack of illumination from some propagation directions we need to migrate roughly 2000 plane waves. This

means that 3D-PERM data size can be one order of magnitude smaller than 3D-plane wave data.

Despite the recent good migration results obtained in geologically complex areas using wide-azimuth data, narrow-azimuth acquisition is still the industry standard. Narrow-azimuth data can be efficiently imaged by common-azimuth wave-equation migration (CAM) (Biondi and Palacharla, 1996). That is because the dimensionality of the pre-stack wavefields is decreased by assuming zero cross-line offset in contrast with the full-azimuth migration. That does not mean that the cross-line offset wavenumber is zero. Rather, its asymptotic approximation is a function of the in-line midpoint and in-line offset wavenumbers. Therefore, instead of a five-dimensional hypercube, CAM images are four-dimensional hypercubes in \mathbf{x} and h_x .

Because of the lower dimensionality of CAM images, when using them as the initial conditions to synthesize PERM data, the SODCIGs in the cross-line direction can be sampled continuously, as depicted in Figure 2.20b. Contrast this case with the five-dimensional initial conditions for the full azimuth case of Figure 2.20a. Recall that PERM is equivalent to ERM if energy is focused at the zero subsurface offset, as well as if this is the only available subsurface offset.

The continuous sampling of SODCIGs in the cross-line direction yields one more order of magnitude of data reduction. Therefore, under the common-azimuth approximation, 3D-PERM data size can be two orders of magnitude smaller than 3D-plane wave data.

To illustrate the validity of the above assumptions, a split-spread data with maximum offset of 1587.5 m was computed using 3D-Born modeling (Rickett et al., 1996) on a 30° dipping reflector with 45° azimuth with respect to the acquisition direction, which is aligned with the in-line direction. There are 96 in-lines and cross-lines spaced 25 m apart. The offset interval is 25 m. The velocity used in the modeling is the 1D function $v(z) = (1500 + 0.5z)$ m/s.

The Born data was input to CAM with a 5% slower velocity. Migration results can be seen in Figures 2.21a and 2.21b for SODCIGs positioned at $(x = 750 \text{ m}, y = 600$

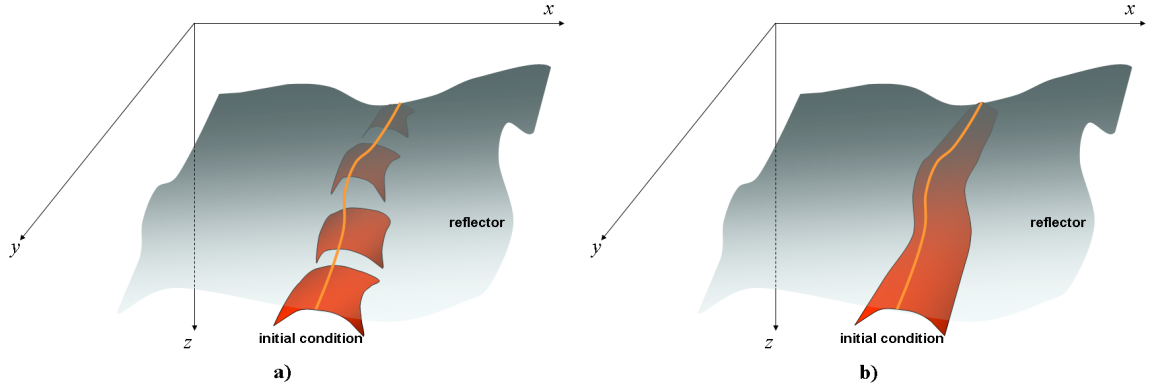


Figure 2.20: The initial conditions for synthesizing PERM data from CAM images can be specified as in b) because no pre-stack information exists in the cross-line direction, in contrast with the full azimuth situation in a). `perm/.cam01`

m) and $(x = 750 \text{ m}, y = 1000 \text{ m})$, respectively. The panel on the left is the SODCIG, which contains 21 subsurface offsets ranging from -250 m to 250 m . The panel in the middle is the in-line at zero subsurface offset, with $y = 600 \text{ m}$ (Figure 2.21a) and $y = 1000 \text{ m}$ (Figure 2.21b). The panel on the right is the cross-line at zero subsurface offset, with $x = 750 \text{ m}$.

In the common-azimuth regime, the computation of the dip-independent initial conditions is performed by simply rotating the SODCIGs in the in-line direction, since no cross-line offset is computed in migration. The underlying assumption that source and receiver rays cross, which makes the rotation valid in 3D, implies that they are coplanar. This assumption is in agreement with the co-planarity condition present in the formulation of CAM.

Source and receiver wavefields were modeled using continuous sampling along the cross-line direction and sampling period of 48 in the in-line direction. This period is sufficient to avoid crosstalk during the areal-shot migration, given that the number of subsurface-offsets of the pre-stack image is 21. The synthesized 3D receiver wavefield is shown in Figure 2.22. The left panel is the in-line at $y = 1200 \text{ m}$, the right panel

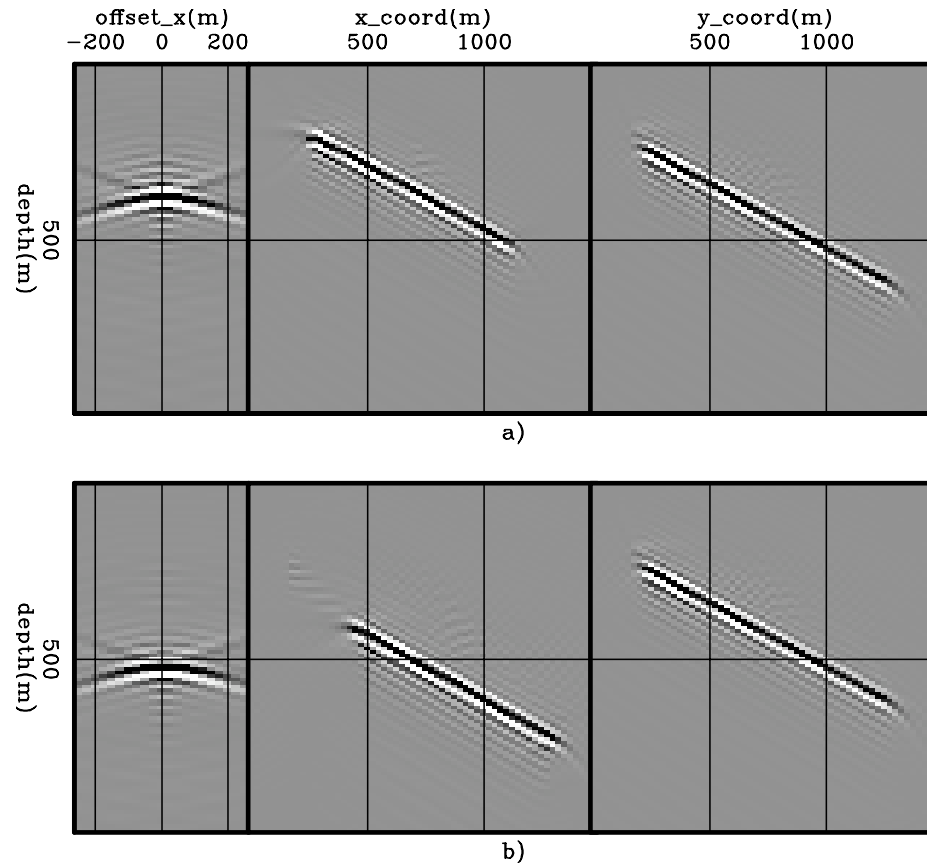


Figure 2.21: Common-azimuth migration of 3D-Born data modeled from a 30° dipping reflector with 45° azimuth with respect to the acquisition direction. The panel in the middle is the in-line at the zero-subsurface offset, and $y = 600$ m (Figure 2.21a) and $y = 1000$ m (Figure 2.21b). The panel on the right is the cross-line at the zero-subsurface offset, and $x = 750$ m. perm/. cam02

is the cross-line at $x = 1400$ m, and the top panel is the time-slice at $t = 0.5$ s.

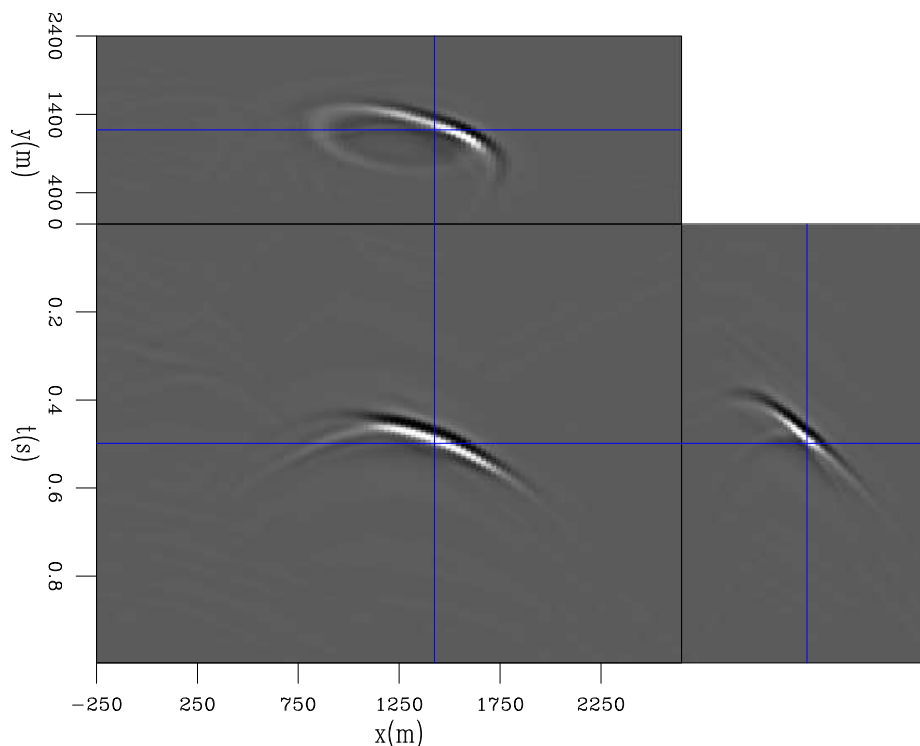


Figure 2.22: 3D-PERM receiver wavefield. The left panel is the in-line at $y = 1200$ m, the right panel is the cross-line at $x = 1400$ m, and the top panel is the time-slice at $t = 0.5$ s. perm/. cam03

The 3D migration of the 48 areal shots with the velocity underestimated by 5% is shown in Figures 2.23a and 2.23b for SODCIGs positioned at $(x = 750$ m, $y = 600$ m) and $(x = 750$ m, $y = 1000$ m), respectively. To facilitate the comparison with the CAM images of Figures 2.21a and 2.21b, the polarity of the areal-shot migrated image is inverted because of the squaring of the wavelet. The kinematics of the SODCIGs computed with PERM wavefields matches those of the SODCIGs computed with CAM, especially between -200 m and 200 m. This enables the use of 3D PERM wavefields computed from CAM images in optimization of migration velocity, as will be shown in Chapter ?? for a 3D survey from the North-Sea.

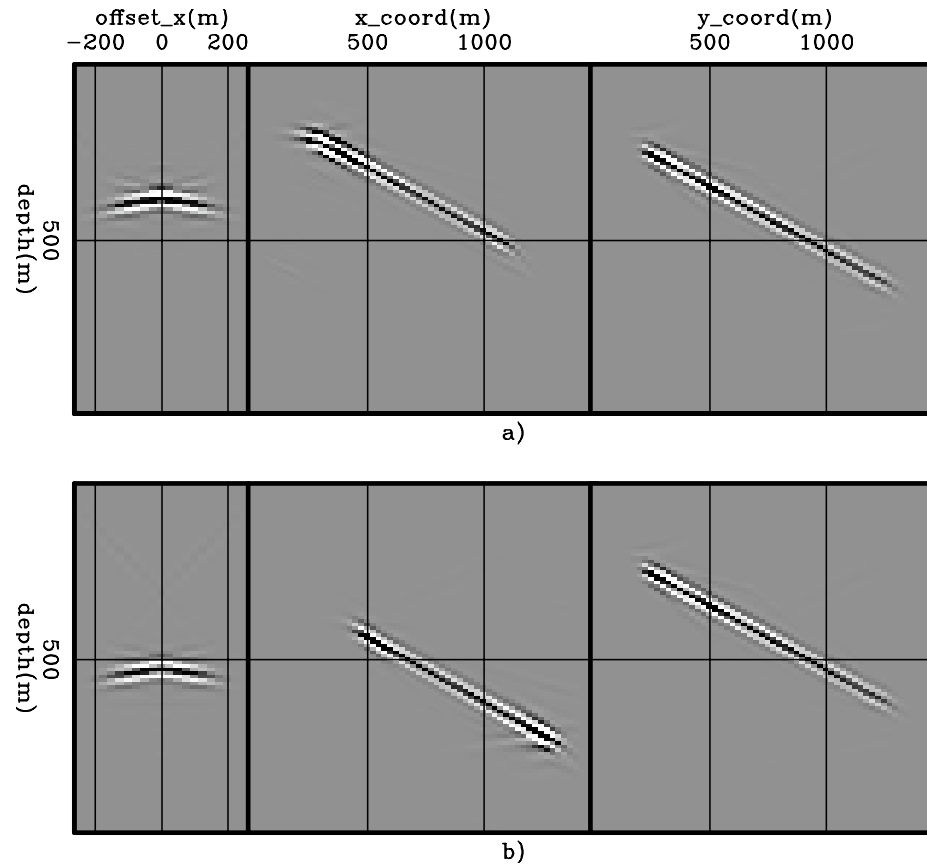


Figure 2.23: 3D-areal-shot migration of PERM data. The panel in the middle is the in-line at the zero-subsurface offset, and $y = 600$ m (Figure 2.21a) and $y = 1000$ m (Figure 2.21b). The panel on the right is the cross-line at the zero-subsurface offset, and $x = 750$ m. Compare with Figure 2.21. perm/. cam04

CONCLUSIONS

In this chapter we saw that wavefields synthesized by PERM can provide migrated images with correct kinematics while decreasing data size. Data reduction is achieved by combining the modeling experiments and is controlled by the number of subsurface offsets that will be computed during areal-shot migration of PERM data. Recall that SODCIGs in the initial conditions must be separated by at least twice the maximum absolute subsurface-offset value to prevent crosstalk. Implicit to PERM is that reflectors must be identified such that reflector crosstalk is avoided during migration. 3D Pre-stack interpretation can be cumbersome, but it allows, for instance, avoiding the use of reflectors with low signal-to-noise ratios in migration velocity estimation. Moreover, in commercial softwares for migration velocity estimation reflector picking is a standard and almost entirely automated procedure.

Whereas in 2D, PERM data size is comparable to that of the plane-wave decomposition, in 3D it can be one order of magnitude smaller if cross-line subsurface-offsets are to be computed. Further data size reduction by one order of magnitude is achieved if the initial conditions are computed with common-azimuth migration.

Bibliography

- Berkhout, A. J., 1997a, Pushing the limits of seismic imaging, PART I: Prestack migration in terms of double dynamic focusing: *Geophysics*, **62**, 937–953.
- , 1997b, Pushing the limits of seismic imaging, PART II: Integration of prestack migration, velocity estimation, and avo analysis: *Geophysics*, **62**, 954–969.
- Billette, F., G. Lambare, and P. Podvin, 1997, Velocity macromodel estimation by stereotomography: *SEG Technical Program Expanded Abstracts*, **16**, 1889–1892.
- Biondi, B., 2006, Prestack exploding-reflectors modeling for migration velocity analysis: *SEG Technical Program Expanded Abstracts*, **25**, 3056–3060.
- Biondi, B., S. Fomel, and N. Chemingui, 1998, Azimuth moveout for 3-D prestack imaging: *Geophysics*, **63**, 574–588.
- Biondi, B. and G. Palacharla, 1996, 3-D prestack migration of common-azimuth data: *Geophysics*, **61**, 1822–1832.
- Biondi, B. and G. Shan, 2002, Prestack imaging of overturned reflections by reverse time migration: *SEG Technical Program Expanded Abstracts*, **21**, 1284–1287.
- Biondi, B. and W. W. Symes, 2004, Angle-domain common-image gathers for migration velocity analysis by wavefield-continuation imaging: *Geophysics*, **69**, 1283–1298.
- Black, J. L. and M. S. Egan, 1988, True-amplitude DMO in 3-D: *SEG Technical Program Expanded Abstracts*, **7**, 1109–1112.
- Bleistein, N., J. Cohen, and H. Jaramillo, 1999, True-amplitude transformation to zero offset of data from curved reflectors: *Geophysics*, **64**, 112–129.
- Claerbout, J., 1985, *Imaging the Earth’s Interior*: Blackwell Scientific Publications.
- Claerbout, J. F., 1971, Toward a unified theory of reflector mapping: *Geophysics*, **36**,

- 467–481.
- Cruz, J. C. R., P. Hubral, M. Tygel, J. Schleicher, and G. Höcht, 2000, The common reflecting element (CRE) method revisited: *Geophysics*, **65**, 979–993.
- Fei, W., P. Williamson, and A. Khoury, 2009, 3-D common-azimuth wave-equation migration velocity analysis: *SEG Technical Program Expanded Abstracts*, **28**, 2283–2287.
- Gelchinsky, B., 1988, The common reflecting element (CRE) method (non-uniform asymmetric multifold system): *Exploration Geophysics*, **19**, 71–75.
- Hale, D., 1984, Dip-moveout by fourier transform: *Geophysics*, **49**, 741–757.
- Kapoor, S. J., M. O’Brian, D. Desta, I. Atakishiyev, and M. Tomida, 2007, Subsalt imaging — the raz/waz experience: *SEG Technical Program Expanded Abstracts*, **26**, 926–930.
- Kosloff, D., J. Sherwood, Z. Koren, E. Machet, and Y. Falkovitz, 1996, Velocity and interface depth determination by tomography of depth migrated gathers: *Geophysics*, **61**, 1511–1523.
- Kosloff, D., U. I. Zackhem, and Z. Koren, 1997, Subsurface velocity determination by grid tomography of depth migrated gathers: *SEG Technical Program Expanded Abstracts*, **16**, 1815–1818.
- Liner, C. L., 1991, Born theory of wave-equation dip moveout: *Geophysics*, **56**, 182–189.
- Loewenthal, D., L. Lu, R. Roberson, and J. Sherwood, 1976, The wave equation applied to migration: *Geophysical Prospecting*, **24**, 380–399.
- Moldoveanu, N., J. Kapoor, and M. Egan, 2008, Full-azimuth imaging using circular geometry acquisition: *The Leading Edge*, **27**, 908–913.
- Peles, O., A. Bartana, D. Kosloff, and Z. Koren, 2004, Limitations of the exploding reflector model in sub-salt imaging: *SEG Technical Program Expanded Abstracts*, **23**, 2455–2457.
- Regone, C. J., 2007, Using 3d finite-difference modeling to design wide-azimuth surveys for improved subsalt imaging: *Geophysics*, **72**, SM231–SM239.
- Rickett, J., B. Biondi, and D. Lumley, 1996, Modeling heterogeneous reservoirs using the first order Born approximation: **SEP-92**, 75–82.

- Rickett, J. E. and P. C. Sava, 2002, Offset and angle-domain common image-point gathers for shot-profile migration: *Geophysics*, **67**, 883–889.
- Rietveld, W. E. A. and A. J. Berkhout, 1992, Prestack depth migration by means of controlled illumination: *Geophysics*, **59**, 801–809.
- Rietveld, W. E. A., A. J. Berkhout, and C. P. A. Wapenaar, 1992, Optimum seismic illumination of hydrocarbon reservoirs: *Geophysics*, **57**, 1334–1345.
- Romero, L., D. Ghiglia, C. Ober, and S. Morton, 2000, Phase encoding of shot records in prestack migration: *Geophysics*, **65**, 426–436.
- Sava, P. C. and S. Fomel, 2003, Angle-domain common-image gathers by wavefield continuation methods: *Geophysics*, **68**, 1065–1074.
- Stork, C., 1992, Reflection tomography in the postmigrated domain: *Geophysics*, **57**, 680–692.
- Thorbecke, J. and A. J. Berkhout, 2006, Recursive prestack depth migration using CFP gathers: *Geophysics*, **71**, S273–S283.
- Tygel, M., J. Schleicher, P. Hubral, and L. T. Santos, 1998, 2.5-D true-amplitude kirchhoff migration to zero offset in laterally inhomogeneous media: *Geophysics*, **63**, 557–573.